Synthesis of Centimeter-Scale Monolayer Tungsten Disulfide Film on Gold Foils

Seok Joon Yun,[†,‡,#] Sang Hoon Chae,[†,#] Hyun Kim,[†,‡] Jin Cheol Park,[†,§] Ji-Hoon Park,[†] Gang Hee Han,[†] Joo Song Lee,[⊥] Soo Min Kim,[⊥] Hye Min Oh,[†,‡] Jinbong Seok,[†,‡] Mun Seok Jeong,[†,‡] Ki Kang Kim,*[,∥] and Young Hee Lee*[,†,‡,§]

[†]IBS Center for Integrated Nanostructure Physics, Institute for Basic Science (IBS), Sungkyunkwan University, Suwon 440-746, Republic of Korea, [‡]Department of Energy Science and [§]Department of Physics, Sungkyunkwan University, Suwon 440-746, Republic of Korea, [⊥]Institute of Advanced Composite Materials, Korea Institute of Science and Technology (KIST), San101 Eunha-Ri, Bongdong-Eup, Wanju-Gun, Jeollabuk-Do 565-902, Republic of Korea, and [∥]Department of Energy and Materials Engineering, Dongguk University—Seoul, Seoul 100-715, Republic of Korea. [#]These authors contributed equally

ABSTRACT

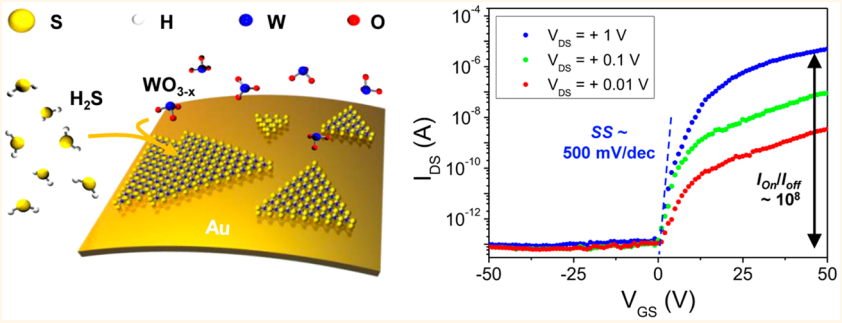

We report the synthesis of centimeter-scale monolayer WS_2 on gold foil by chemical vapor deposition. The limited tungsten and sulfur solubility in gold foil allows monolayer WS_2 film growth on gold surface. To ensure the coverage uniformity of monolayer WS_2 film, the tungsten source-coated substrate was placed in parallel with Au foil under hydrogen sulfide atmosphere. The high growth temperature near 935 °C helps to increase a domain size up to 420 μm. Gold foil is reused for the repeatable growth after bubbling transfer. The WS_2-based field effect transistor reveals an electron mobility of 20 $cm^2 V^{-1} s^{-1}$ with high on−off ratio of ~10^8 at room temperature, which is the highest reported value from previous reports of CVD-grown WS_2 samples. The on−off ratio of integrated multiple FETs on the large area WS_2 film on SiO_2 (300 nm)/Si substrate shows within the same order, implying reasonable uniformity of WS_2 FET device characteristics over a large area of 3 × 1.5 cm^2.

KEYWORDS: tungsten disulfide · chemical vapor deposition · transition metal dichalcogenides · gold · field effect transistor · bubbling transfer

Unlike graphene, two-dimensional semiconducting transition metal dichalcogenides (s-TMdCs), MX_2 (M = Mo, W; X = S, Se) have various energy band gaps ranging from 1 to 2 eV that reveal peculiar layer-dependent optical transitions.[1−6] Monolayer MoS_2 has shown high mobility of ~50 $cm^2 V^{-1} s^{-1}$, implying that this material can be used in high-speed switching devices with high transmittance and flexibility.[7−10] In particular, the photoluminescence (PL) quantum yield of monolayer WS_2 on quartz has been reported to be as high as ~2.0%, which is much higher than that of suspended monolayer MoS_2 (0.42%).[11] This implies that monolayer WS_2 is a good candidate material for two-dimensional optoelectronic devices.[11−13] Furthermore, the carrier mobility of WS_2 is comparable to that of MoS_2, suggesting that monolayer WS_2 can be applied to thin-film transistors.[14−18] Nevertheless, these studies have been limited to a few μm sizes of samples which are prepared by mechanical exfoliation, hindering further applications.[12,16]

Several methods including liquid exfoliation and chemical vapor deposition (CVD)

* Address correspondence to leeyoung@skku.edu, kkkim@dongguk.edu.

Received for review March 11, 2015 and accepted April 14, 2015.

Published online April 14, 2015
10.1021/acsnano.5b01529

have been reported to obtain monolayer or few-layers WS_2. Liquid exfoliation has an advantage for mass production and is mostly applied to hydrogen evolution reactions;[19,20] however, difficulties exist in controlling defects, limiting its application to electronic devices. CVD is counted as one of the promising method to synthesize WS_2 film because of its scalability and wide tunability in growth parameters of pressure, temperature and source. In a more systematic approach, different strategies for supplying metal sources are adopted before sulfurization in CVD: (i) tungsten or solid tungsten oxide thin-film with various thicknesses and (ii) vaporized solid precursors. Large-area WS_2 thin-film is obtained by a simple sulfurization of thin tungsten film or thin tungsten oxide film deposited by various methods including e-beam evaporation, magnetron sputtering, and atomic layer deposition.[21−26] Although these approaches show wafer-level uniformity, the grain-size of WS_2 film is limited to nanoscale (30−50 nm), which causes the degradation of electrical properties of WS_2 film. Another method is that tungsten oxides and solid sulfur sources are vaporized simultaneously on the insulating substrate (silicon dioxide, sapphire, or hexagonal boron nitride) during CVD process.[27−31] This approach seems to be appropriate for monolayer WS_2 growth with a few tens of micrometers of domains. However, it is still difficult to realize a full coverage of monolayer WS_2 in large areas without additional multilayers. Although the amount of each species is well controlled with a two-zone furnace, vaporization of sources during growth cannot be avoided due to poor adhesion of the sources to insulating substrate, limiting the full coverage of monolayer WS_2 growth. To improve poor adhesion, perylene-3,4,9,10-tetracarboxylic acid tetrapotassium salt (PTAS) or graphite oxide as seeding promoter has been introduced.[32−34] However, although the coverage was much improved, the seeding promoter layer is left over on the substrate after growth, which produces impurities and hinders formation of a continuous film.[33,34]

Another approach is to use a metal substrate instead of an insulating substrate. Metal substrate is advantageous for high catalytic reactivity with precursors.[35] However, special care is required with this approach due to the formation of metal compound or metal alloy. For example, copper foil reacts with sulfur to form CuS_2 at high temperature, disturbing the growth of WS_2 layers on it. Recently, Au substrate has been used for the synthesis of MoS_2.[36−38] Patterned Au thin film was introduced for the synthesis of more than bilayer MoS_2 film *via* the precipitation of Mo atoms in Au bulk.[38] On the other hand, Au foil was applied to synthesize monolayer MoS_2.[36,37] The MoS_2 domain in size was achieved around 80 μm. However, the coverage of monolayer MoS_2 gradually varied with the separation distance from the source. Au substrate has never been applied for large-area WS_2 growth yet.

Here, we report the synthesis of centimeter-scale monolayer WS_2 film with uniform coverage by CVD. We vaporize a tungsten precursor, ammonium metatungstate (AMT, $(NH_4)_6H_2W_{12}O_{40}\cdot x(H_2O)$), which is water-soluble on Au substrate. This combination is certainly advantageous for improving adhesion of precursors. AMT is efficiently converted to W source by catalytic decomposition of WO_x on Au substrate, while Au as a catalyst remains intact. The AMT precursor was uniformly deposited on Au substrate by arranging AMT-loaded alumina substrate in parallel to Au substrate, which is the key to maintain uniform coverage of monolayer WS_2 film over a whole region in centimeter scale. The high growth temperature around 935 °C helps to increase a domain size up to ~420 μm. The grown WS_2 monolayer was transferred to the SiO_2/Si using a PMMA-assisted bubbling transfer method[39,40] or wet-etching method. The fabrication of field effect transistors (FET) revealed an electron mobility of 20 $cm^2\ V^{-1}\ s^{-1}$ with a high on−off ratio of ~10^8 at room temperature, outperforming the previously reported value of ~4 $cm^2\ V^{-1}\ s^{-1}$ from the CVD-grown WS_2 film.[22] The on−off ratio from integrated multiple FETs on centimeter WS_2 film shows within the same order, implying reasonable uniformity of WS_2 FET device. This opens a possibility for large-scale integration of logic circuits using CVD-grown large-area WS_2 film.

RESULTS AND DISCUSSION

To synthesize monolayer WS_2 film on Au foil, a CVD system equipped with a one-zone furnace is introduced, as illustrated in Figure 1a, which is different from previous works conducted with a two-zone furnace.[24,29] Hydrogen sulfide gas as a sulfur source and AMT as a tungsten precursor were used (see Supporting Information Figure S1). AMT was dissolved in deionized water and dropped onto an Al_2O_3 substrate, followed by drying in an oven. To ensure the coverage uniformity of monolayer WS_2 films, several geometries between solid tungsten source and Au foil have been tried (see Supporting Information, Figure S1b). The most promising geometry is the Au foil placed in parallel on top of the precursor substrate, as shown in Figure 1a (see Supporting Information, Figures S1−S4). The growth was normally performed at a high temperature (935 °C) to increase a domain size. Scanning electron microscopy (SEM) images in Figure 1b-e displays the growth behavior of WS_2 on Au foil over time. The triangular island of WS_2 domains were formed within the first 5 min. We notice that WS_2 can grow across Au grain boundaries, as indicated by the white-dotted line in Figure 1b. This indicates that WS_2 is synthesized through surface-mediated growth on a Au surface. With longer growth time (15 min), a complete WS_2 film was formed without an empty region (Figure 1d). The whole area of Au foil was

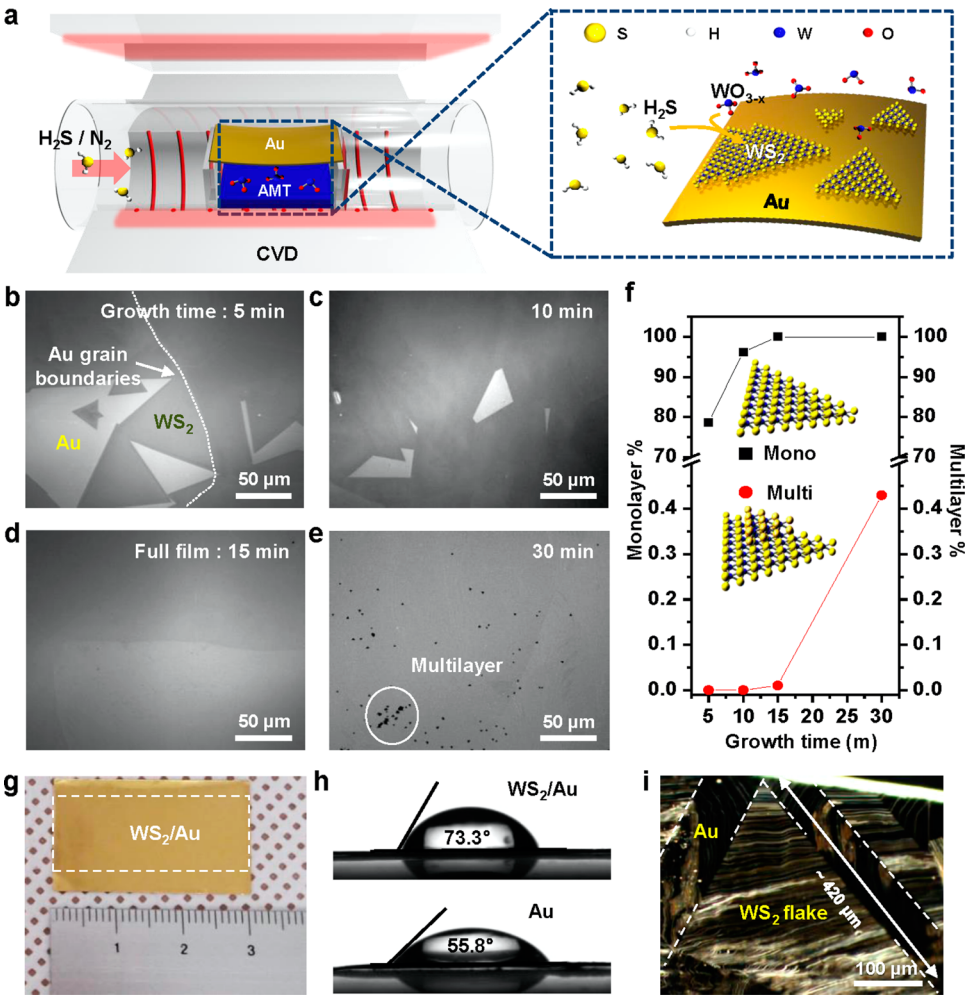

Figure 1. Growth of centimeter-scale monolayer WS_2 film on gold foil. (a) Schematic diagram of the chemical vapor deposition setup and illustration of the growth behavior of WS_2 on Au foil. (b–e) SEM images of WS_2 as a function of growth time: 5, 10, 15, and 30 min, respectively. The white dotted line in (b) indicates the grain boundary of Au. The white circle in (f) highlights some multilayer flakes. (f) Coverage of monolayer and multilayer WS_2 on Au foils. (g) Photograph of WS_2 on Au foils after complete growth. The area of WS_2 film is 6 cm^2. (h) Contact angles before (bottom) and after (top) growth of WS_2 on Au foils. (i) Dark field optical image of WS_2 flakes on Au foils. The domain size is 420 μm.

covered by a monolayer WS_2, which was confirmed by observing several regions with SEM (see Supporting Information, Figures S4 and S5). After 30 min of growth, multilayer flakes were grown over some portion of the monolayer (Figure 1e). As indicated in Figure 1f, monolayer coverage was nearly complete at 15 min and was saturated after 15 min. On the other hand, the multilayer portion slightly increased to 0.4% at 30 min (coverage information was extracted by conventional software, see Supporting Information, Figure S6). The small portion of multilayer after one layer of monolayer growth indicates the surface-mediated growth and catalytic effect of the Au substrate. In addition, the surface morphology of Au foil was found to be very important for the synthesis of monolayer WS_2 (see Supporting Information, Figure S7). A high proportion of multilayer WS_2 islands was observed when WS_2 was grown on bare Au foil. However, after the surface treatments including annealing, chemical mechanical polishing, and acid treatment, the monolayer WS_2 film was predominantly grown. Therefore, the growth of WS_2 was conducted after the surface treatments of Au foil in this work (see Supporting Information, Figure S7).

Figure 1g shows a photograph of WS_2 film on Au foil over an area of 6 cm^2. To observe the change in surface properties after complete growth, the contact angle was measured on both surfaces. As shown in Figure 1h, contact angles of 55.8° and 73.3° on the bare Au and WS_2/Au were observed, respectively, indicating that the surface moves toward a hydrophobic state due to the presence of continuous monolayer WS_2. The dark-field (DF) mode in optical microscopy helps to identify the WS_2 domains on Au foil. DF mode involves detection of scattered light, which is useful for observing rough surfaces. Figure 1i exhibits the DF image of WS_2 domains indicated by the white-dashed line in the initial growth stage. After growth of the WS_2 on Au foil, the gold surface underneath WS_2 domains became rough because of different reconstruction behavior of Au,[41] clearly distinguishing from the bare Au region

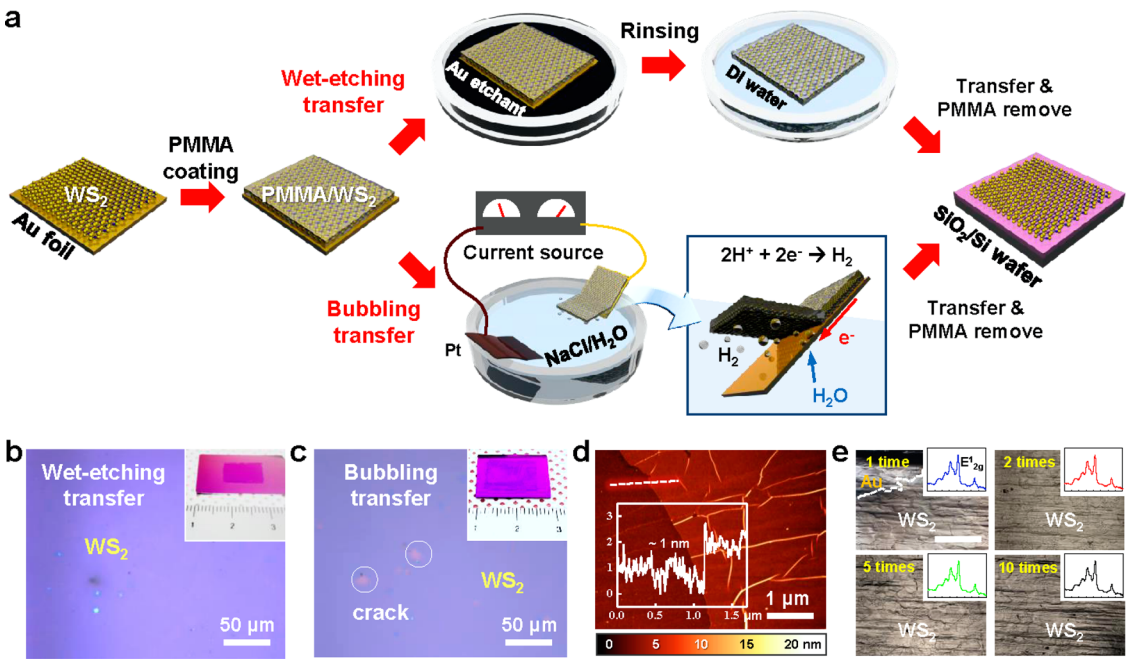

Figure 2. Transfer of WS_2 film to the arbitrary substrate. (a) Schematic diagrams of wet-etching and bubble transfer. After coating PMMA on WS_2/gold foils, PMMA/WS_2 film was obtained in two different ways: wet-etching and bubble transfer. The obtained films were transferred onto the target substrate. (b and c) Optical images of WS_2 films on 300 nm/Si substrate prepared by wet-etching and bubble transfer, respectively. The insets in (b) and (c) are the photographs corresponding to each method. (d) AFM image of WS_2 film on the substrate. The inset shows the height profile of the WS_2 film along the white dashed line in (d). (e) Optical images after repeated growth: first, second, fifth, and 10th time after bubble transfer. The inset of each image shows representative Raman spectra of the WS_2 film corresponding to each growth cycle. All Raman spectra are similar to each other.

(see Supporting Information, Figure S8). The maximum size of WS_2 domains in this study was ~420 μm at 935 °C, which was modulated with growth temperature (see Supporting Information, Figure S9). The elemental analysis after growth was conducted using X-ray photoelectron spectroscopy (XPS) (see Supporting Information, Figure S10). The core level spectra of W 4f and S 2p for WS_2 film were clearly detected. The stoichiometry of tungsten and sulfur was obtained to be around 1:2.[22]

For further measurement of WS_2 film, the WS_2 film was transferred to a SiO_2 substrate. Wet-etching and bubbling transfers were tried,[36] as shown in Figure 2a. To prevent damage to the WS_2 film during the transfer process, a PMMA supporting layer was spin-coated onto the WS_2/Au foil. For wet-etching transfer, Au foil was etched away by the Au etchant. The PMMA/WS_2 film floating on DI water was transferred to the target substrate. This method does not allow reuse of Au foil, which could be a limiting factor for real applications due to the high cost of Au foil. Compared with wet-etching transfer, bubbling transfer has a cost advantage because the Au foil can be reused to grow the WS_2 film after transfer.[39] To conduct the bubbling transfer, WS_2 film on Au foil as a negatively charged cathode was immersed in NaCl solution. Hydrogen bubbles are generated according to the reaction $2H_2O(l) + 2e^- \rightarrow H_2(g) + 2OH^-(aq)$, between WS_2 film and Au surface which eventually delaminates the PMMA-coated WS_2 film from Au foil. The PMMA/WS_2 film was transferred onto the SiO_2/Si substrate.

Figure 2b,c shows optical images of WS_2 film on SiO_2/Si substrate, prepared by wet-etching and bubbling transfers,[39] respectively. The WS_2 film is mostly continuous over the whole area for wet-etching transfer. The inset of Figure 2b shows a photograph of large-area WS_2 film (2 cm^2) on a SiO_2/Si substrate. However, Figure 2c and its inset exhibit an optical image and photograph of WS_2 film on SiO_2/Si transferred by the bubbling method, respectively. The optical image is similar to that of the wet-etching process, but some empty portions were often visible, which requires a special care to be free of this (see Supporting Information, Figure S11). Figure 2d displays the representative AFM image of WS_2 film after it is transferred to the SiO_2/Si substrate. The inset of Figure 2d displays the height profile along the white-dashed line in Figure 2d, indicating that the 1 nm-thick WS_2 film is indeed a monolayer. Moreover, the wrinkles formed during transfer process were clearly observed (MoS_2/Au).[36,37] To demonstrate the advantage of the bubbling transfer, the regrowth of WS_2 on Au foils after both bubbling transfer and the cleaning process (see Supporting Information, Figure S12) were carried out. Figure 2e displays the optical images of WS_2 films on Au foil after up to 10 repeated growth cycles, with corresponding Raman spectra on WS_2/Au foils, demonstrating that Au foil can be reused for repeatable growth.[39]

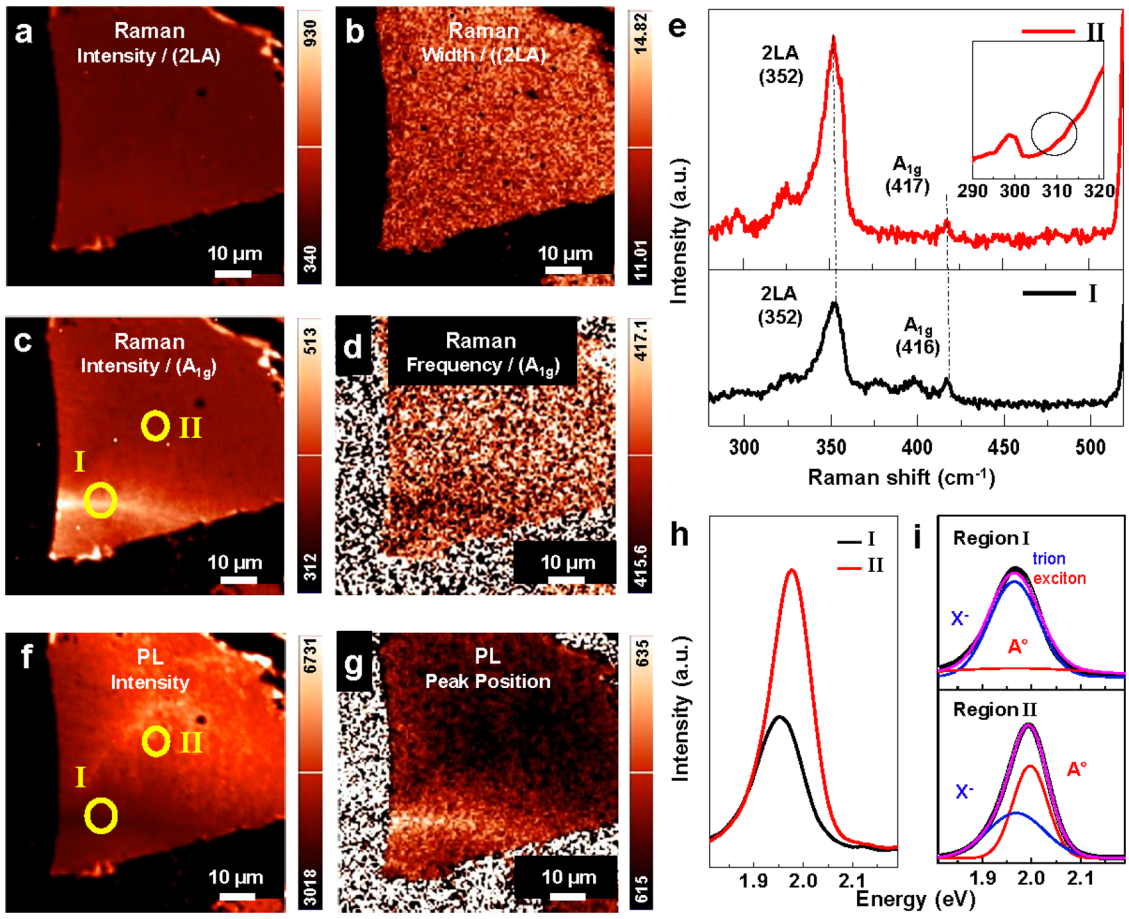

Figure 3. Optical properties of WS_2 film transferred onto SiO_2/Si substrate. (a–d) 2D Raman mapping images of WS_2 film for (a) the intensity of 2LA, (b) fwhm of 2LA, (c) the intensity of A_{1g}, and (d) the peak position of A_{1g} peak frequency (415.6–417.1 cm^{-1}), respectively. at the same region with 532 nm laser excitation. (e) Representative Raman spectra at region I and II in (c). The inset shows Raman active mode (B^1_{2g}) for multilayer WS_2, indicating only monolayer WS_2. (f and g) 2D PL mapping images for (f) PL intensity and (g) PL peak position (615–635 nm) with 532 nm excitation laser. (h) Representative PL spectra of region I and II in (f). (i) The deconvoluted PL spectra into neutral exciton (A°) and trion (X^-) for each region.

To estimate the optical properties and quality of the transferred monolayer WS_2 film on SiO_2/Si substrate, the sample was characterized by Raman spectroscopy and PL. Raman spectroscopy has been used for determining the strain, doping effect, and thickness.[42−47] Figure 3a,b displays Raman mapping images for the intensity and full width at half-maximum (fwhm) of 2LA (~352 cm^{-1}).[30] A uniform contrast in both intensity and fwhm mapping images was observed, implying that the transferred monolayer WS_2 film has uniform thickness and crystallinity over the whole area. The fwhm of our sample is 4.2 cm^{-1}, which is comparable to the value (3.8 cm^{-1}) of exfoliated monolayer WS_2 flake (see Supporting Information Figure S13). This result supports that our sample has reasonable crystal quality, compared to exfoliated sample. On the other hand, Raman mapping image for the intensity and position of A_{1g} mode (~417 cm^{-1}) in Figure 3c,d displays the uniform intensity and fwhm except for a specific broad line in the bottom left region I. To understand why the intensity or position of A_{1g} mode is different at region I and II in Figure 3c, Raman spectra were carefully analyzed further. Figure 3e displays the representative Raman spectra of the region I (bottom) and II (top) in Figure 3c. The A_{1g} mode in region I was blue-shifted by ~1 cm^{-1} compared to that in region II. This implies that the region I is more n-type doped than other regions.[46,48] Insets of top panel in Figure 3e show the zoom-in spectra near the B^1_{2g} mode (308 cm^{-1}). The B^1_{2g} phonon is an inactive mode for the monolayer, but is active for multilayers.[49] We could not observe the B^1_{2g} mode in the Raman spectra in our sample, indicating that the WS_2 film is a monolayer in the whole area.

The PL intensity of monolayer WS_2 is in general very strong due to formation of direct bandgap compared to that of multilayer WS_2 of indirect band gap.[21,50,51] In addition, the PL intensity and peak position rely strongly on the doping level.[52,53] Figure 3f,g shows two-dimensional (2D) PL mapping images for the intensity and position of exciton emission near 2 eV, respectively. Both PL images display strong intensity and same peak position over the whole area except for the bottom left region I. This is similar trend to the change of A_{1g} mode in the Raman spectra. Figure 3h

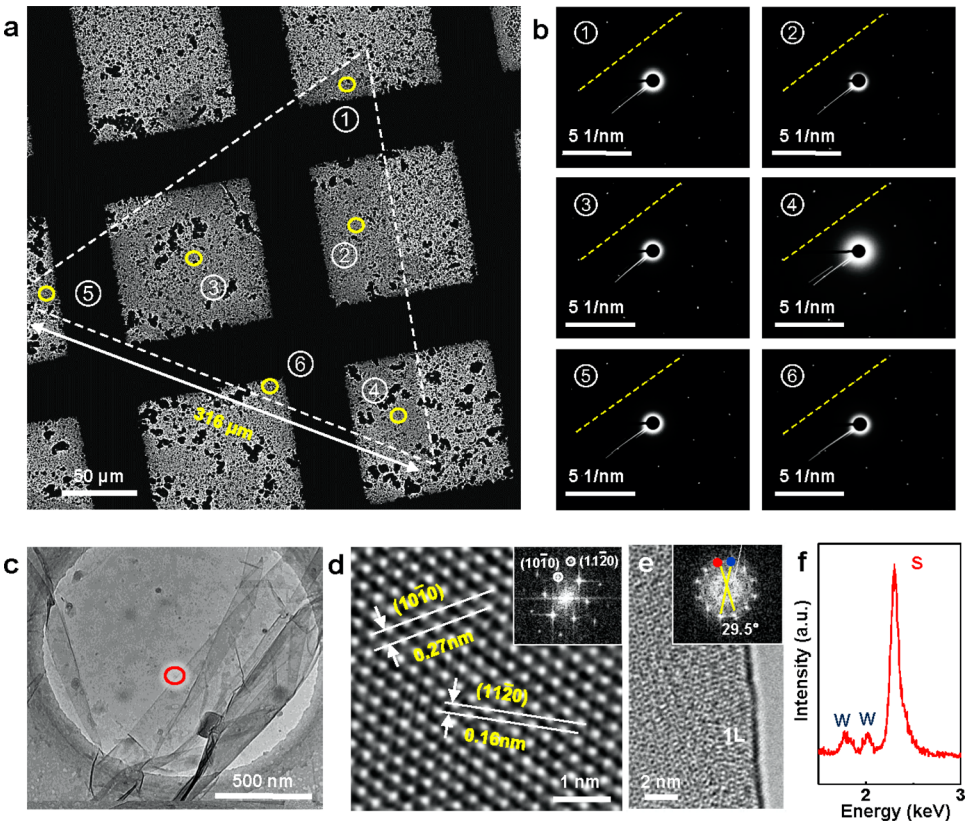

Figure 4. Atomic structure of monolayer WS_2. (a) Low-resolution TEM image of a transferred WS_2 domain on carbon-supported TEM grid. (b) Selective area electron diffraction (SAED) patterns corresponding to the regions of marked numbers in (a). The hexagonal dots from each region have the same orientation within ±1° tolerance, implying that the WS_2 domain is a single crystalline. (c) TEM image of a transferred WS_2 film on a TEM grid. (d) ADF-STEM image of WS_2 film. The inset displays the FFT images corresponding to (d). The planes of (10$\bar{1}$0) and (11$\bar{2}$0) are identified. The interplane distances of (10$\bar{1}$0) and (11$\bar{2}$0) are 2.7 and 1.6 Å, respectively. (e) High-resolution TEM image in the edge of WS_2 film. The inset displays the FFT images of (e). Moiré patterns were observed due to the folded monolayer film with 29.5° rotation. (f) EDX spectrum of WS_2 film from the red circle in (c).

displays the representative PL spectra corresponding to region I and II in Figure 3f. PL intensities and peak positions of the characteristic peak near 2 eV in region I and II are different from each other, where the intensity and position of region I are weaker and red-shifted compared to those of region II. To understand the degradation of PL intensity in region I, the main PL peak was deconvoluted into two Lorentzian peaks; trion (X^-) around 1.96 eV and neutral exciton (A^0) around 2.00 eV.[45] It has been reported that trion was observed with coexisting neutral exciton in n-type MoS_2.[54] When holes (electrons) are injected into n-type MoS_2 or WS_2, neutral exciton emission is dramatically enhanced (suppressed).[45,53] In our case, the intensity of neutral exciton related to peak A^0 was significantly suppressed in region I. This strongly indicates that region I in the sample is n-type doped, correlated with Raman results. The reason why the doping level is different in region I is not clear at this moment. We presume that this n-doping might be caused by chlorine doping[55] introduced during the NaCl bubbling transfer process.

The crystallinity of the monolayer WS_2 was further characterized using transmission electron microscopy (TEM) and annular dark field scanning transmission electron microscopy (ADF-STEM). The crystallinity of the triangular WS_2 domain was identified by a selective-area electron diffraction (SAED) technique using TEM. Figure 4a presents the TEM image of a triangular WS_2 domain (~316 μm) on a carbon-supported TEM grid. Six SAED images corresponding to the numbered regions in Figure 4a illustrate that the hexagonal dots are aligned in a specific direction indicated by yellow-dashed lines (Figure 4b), confirming that the triangular domain is a single crystal. To analyze the atomic arrangement of WS_2 film, the film was transferred to a TEM grid with holes, as shown in Figure 4c. The ADF-STEM image (Figure 4d) clearly shows the lattice fringes of WS_2. The distances of the (10$\bar{1}$0) and (11$\bar{2}$0) planes were identified by a fast Fourier transform (FFT) image as shown in the inset of Figure 4d and were found to be 0.27 and 0.16 nm, in good agreement with known values.[22,29] Monolayer WS_2 film was confirmed by counting the folded edge of the layer (Figure 4e). In addition, a moiré pattern in the folded monolayer film was observed due to the misorientation of two monolayers after folding. The twist angle was confirmed by

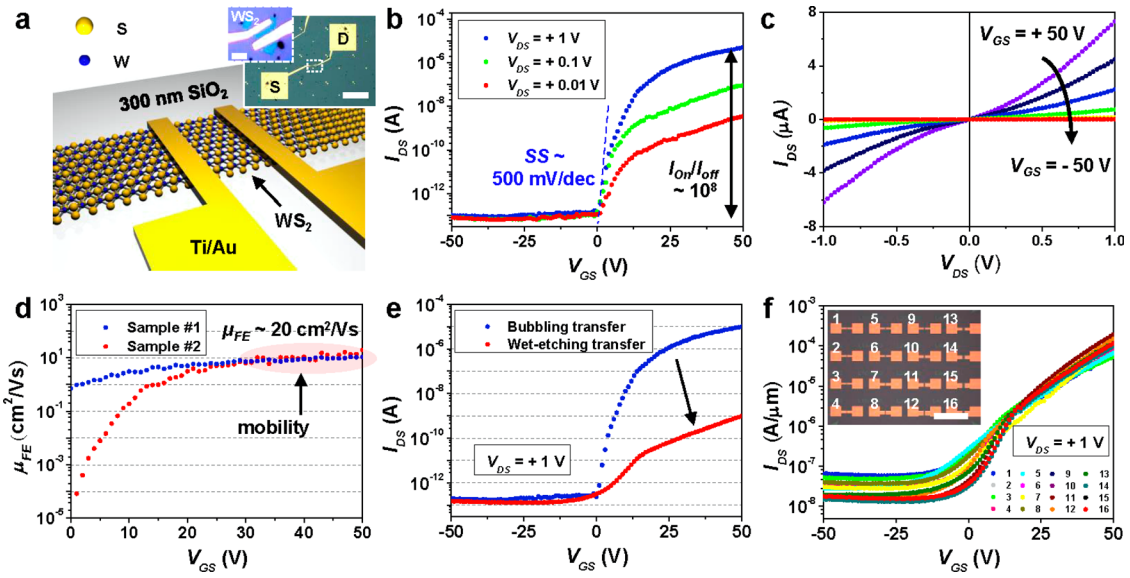

Figure 5. Electrical properties of monolayer WS_2 film. (a) Schematic illustration of a back-gated WS_2-field effect transistor (FET) on SiO_2/Si substrate. The insets are optical images of the real WS_2−FET structure. The scale bars in low (large one) and high (small one) magnitude image are 200 and 5 μm, respectively. (b) Transfer characteristic of WS_2−FET as a function of gate voltage. The samples were fabricated by e-beam lithography technique. (c) Drain current−voltage curves with different gate voltages from −50 to 50 V in steps of 10 V. The nonlinear curve indicates a Schottky barrier between the electrode and WS_2. (d) Extracted field-effect mobility as a function of gate voltage. The red shaded circle indicates the range of mobility in the linear regime. (e) Dependence of $I-V$ characteristic on the transfer method: wet-etching and bubbling transfer. (f) Electrical characteristics as a function of gate voltage in a WS_2−FET array, prepared using a conventional photolithography technique. The inset displays the real WS_2−FET array. The numbers in the caption correspond to each WS_2−FET in the inset. All $I-V$ curves are nearly identical. The scale bar in the inset indicates 500 μm.

the FFT image in the inset of Figure 4e. The two sets of hexagonal spots were rotated by 29.5°. The chemical elements of tungsten and sulfur were detected using energy-dispersive X-ray spectroscopy (EDS) at the red circle in Figure 4c. The stoichiometry of W and S was of a 1:2 ratio. This confirms indeed the existence of a monolayer WS_2 film.

To evaluate the electrical properties of monolayer WS_2 film, field effect transistors were fabricated after the transfer of WS_2 film onto the 300 nm SiO_2/Si substrate (Figure 5a) using bubbling transfer and e-beam lithography. To fabricate an array of WS_2−FETs, a wet-etching transfer method was used. The devices were annealed at 100 sccm of nitrogen gas at 200 °C for 5 h in order to improve contact between the electrodes and WS_2, and also to remove oxygen-related functional groups on the WS_2 surface. The fabricated devices were tested at a vacuum pressure of $\sim 10^{-5}$ Torr at room temperature.

The transfer characteristics of the WS_2−FET were measured within a ± 50 V gate bias, which was applied through a heavily doped Si gate placed underneath the 300 nm SiO_2 dielectric. As shown in Figure 5b, a well-defined n-type switching behavior with a saturated current in the high voltage region was observed, which is in good agreement with PL results. At a V_{SD} of 1 V, a high on/off ratio of $\sim 10^8$ was obtained. The dashed lines in Figure 5b serve as a visual guide to extract the subthreshold swing (SS). A 500 mV/dec SS was extracted when V_{DS} = 1 V. Figure 5c shows $I_{DS}-V_{DS}$ characteristics for gate bias between −50 and +50 V. The curves exhibit nonlinear output characteristics at low biases, indicating that a small Schottky barrier for electron conduction was formed at the Ti/Au contacts. The field effect transistor model: $I_{DS} = \mu_{FE} \cdot C_i \cdot W_{ch} \cdot (1/L_{ch}) \cdot (V_{GS} - V_T) \cdot V_{DS}$, where μ_{FE}, C_i, W_{ch}, L_{ch}, and V_T are the mobility, specific gate capacitance, channel width, channel length, and threshold voltage, respectively, was used to extract the room temperature field-effect mobility μ_{FE}.[56,57] Room-temperature μ_{FE} was extracted from the transfer curve of two samples which were fabricated using e-beam lithography technique. Figure 5d presents the extracted field-effect mobility as a function of gate bias. The maximum electron mobility of sample #2 at room temperature in the linear regime was achieved to be 20.4 $cm^2\ V^{-1}\ s^{-1}$, which is the highest reported value among those of previous reports for CVD-grown WS_2 samples (see Supporting Information Table S1).[22−24] The mobility of sample #1 was 15 cm^2/(V s) in the linear regime. The array of WS_2−FETs was prepared using wet-etching transfer. Wet-etching transfer helps to obtain complete coverage of WS_2 film with no cracks in the film, although this approach degrades the transfer characteristics of WS_2−FETs (Figure 5e). The on-current level decreased to 10^{-9} A when V_{DS} = 1 V was applied, and the mobility value decreased to ~0.1 $cm^2\ V^{-1}\ s^{-1}$, which is lower than that of the bubbling process. It is unclear why the on-current was lowered, but it might be attributed to the damage of WS_2 film by etchant during a long-time

etching process for Au or unintended doping during the transfer process. Although the transfer technique should be improved for various applications, the WS_2—FET array is a still good tool for assessing the uniformity of WS_2 film. For a total of 16 FETs, the dimension of the channel is different for each FET; therefore, I_{DS} is normalized according to channel width. All of the FETs revealed similar transport behavior, as shown in Figure 5f, implying that large-area monolayer WS_2 film has reasonable uniformity.

CONCLUSION

We successfully synthesized WS_2 film on Au foil. Lack of solubility or compound formation with tungsten and sulfur in/with Au bulk helps to synthesize the surface-mediated growth of monolayer WS_2 on Au foil. By placing the source substrate and gold together, the high coverage uniformity (~99%) of monolayer WS_2 film was achieved in a centimeter scale. High growth temperature increases a domain size up to 420 μm. Bubbling transfer has advantages not only to allow for the repeated growth of monolayer WS_2 film, but also to improve the performance of WS_2 FET (to a mobility of ~20 $cm^2\ V^{-1}\ s^{-1}$ and an on—off ratio of $\sim 10^8$). We believe this work sheds light on the synthesis of a large-area monolayer WS_2 film and provides a key idea for the synthesis of other monolayer s-TMdCs.

EXPERIMENTAL SECTION

Synthesis of Monolayer WS_2 Film on Gold Foils. Before synthesis, to smooth the gold surface, Au foil (100 μm, 99.99% iNexus, Inc.) was annealed at 1035 °C for 2 h, followed by chemical mechanical polishing with diluted Au etchant (GE-8148, Transene) in deionized (DI) water. Eight grams of ammonium metatungstate hydrate (AMT, Sigma-Aldrich) as a tungsten source was dissolved in 10 mL of DI water (0.8 g/mL). Twenty microliters of AMT solution was dropped onto an Al_2O_3 plate using a micropipette, and the plate was dried in an oven. The AMT-coated Al_2O_3 plate and Au foil were placed in parallel as shown in Figure 1a and then loaded into a 2-in. CVD chamber. To synthesize WS_2 film on Au foil, the temperature profile was divided into two steps. First, the furnace was heated to 500 °C at a rate of 50 °C/min in a nitrogen atmosphere with a flow rate of 300 sccm and was maintained at 500 °C for 20 min to evaporate the water in AMT. Second, the furnace was further heated to 935 °C and then hydrogen sulfide gas at a rate of 20 sccm for 15 min was supplied. After growth, the temperature was cooled rapidly by opening the furnace.

Wet-Etching and Bubbling Transfers. To prevent damage to the WS_2 film, a PMMA protecting layer was spun onto the WS_2/Au foils, after which the transfers were performed. For the wet-etch transfer, Au foil was etched away using Au etchant (GE-8148, Transene) for 5 h, and then the film was rinsed in DI water several times to remove the residual Au etchant. The resultant film (PMMA/WS_2) was transferred onto the target substrate. For bubbling transfer, PMMA/WS_2/Au foils and platinum as cathode and anode electrode, respectively, were immersed in 1 M NaCl solution. A constant current was applied to generate hydrogen bubbles according to the reaction $2H_2O(l) + 2e^- \rightarrow H_2(g) + 2OH^-(aq)$ at the cathode electrode. The bubbles put pressure on the PMMA/WS_2 film at the Au surface so that it delaminated from the Au foil. The resultant film (PMMA/WS_2) in both cases was transferred to the target substrate (300 nm SiO_2/Si). To remove the PMMA layer, the film was immersed in hot acetone for 10 min.

Characterization Methods. The surface morphology before and after growth was characterized using optical microscopy (Axio imager 2, CARL ZEISS) and field emission SEM (FESEM, JSM7000F, JEOL). The contact angle was measured using water contact measurement (PHX300, Surface Electro Optics). The thickness of WS_2 on 300 nm SiO_2/Si substrate was measured using AFM (SPA 400, SEIKO). The optical properties of WS_2 film were resolved by Raman and PL mapping at an excitation energy of 2.33 eV (NTEGRA-SPECTRA, NT-MDT). ADF-STEM (ARM200F, JEM) and XPS (K-Alpha, THERMO FISHER) were employed to characterize atomic structure and elemental analysis. For TEM measurement, a low acceleration voltage (80 kV) was used to avoid any damage to samples during the observation.

Device Fabrication and Electrical Measurement. After WS_2 was transferred to the Si/SiO_2 (300 nm) *via* bubbling transfer, e-beam lithography and vacuum metallization (Ti/Au, 5/35 nm) were performed to fabricate a single WS_2—FET. To fabricate WS_2-FET array, fully covered WS_2 film was transferred *via* wet-etching transfer to the Si/SiO_2 (300 nm) substrate. The channel and electrode regime were defined using standard photolithography, Reactive Ion Etching (RIE) (SF_6 10 sccm, 20 W, 10 s, All for system), metallization (Ti/Au, 5/35 nm), and lift-off. The WS_2—FET array was further annealed in 100 sccm of nitrogen gas at 200 °C for 5 h in order to remove the residual water. This annealing process also improves the contacts between the channel and electrodes and reduces the contact resistance in the device. Electrical measurements were performed using a probe station (MS tech) and SMU analyzer (Keithley 4200) under vacuum conditions.

Hazards. The use of hydrogen disulfide gas (H_2S) demands great caution because of its toxicity. CVD should be operated inside a fume hood and its exhaust line must be connected to scrubber system to purify H_2S gas.

Conflict of Interest: The authors declare no competing financial interest.

Supporting Information Available: Figure S1—S13, Table S1 and Supporting Information reference. This material is available free of charge *via* the Internet at http://pubs.acs.org.

Acknowledgment. This work was supported by IBS-R011-D1 and in part by the Human Resources Development program (No. 20124010203270) of the Korea Institute of Energy Technology Evaluation and Planning(KETEP) grant funded by the Korea government Ministry of Trade, Industry and Energy. J.S.L. and S.M.K. acknowledge support from the KIST Institutional Program. We would like to thank Prof. Woochul Yang and Soo Ho Choi for assistance regarding the AFM measurement.

REFERENCES AND NOTES

1. Geim, A. K. Graphene: Status and Prospects. *Science* **2009**, *324*, 1530–1534.
2. Geim, A. K.; Grigorieva, I. V. Van der Waals heterostructures. *Nature* **2013**, *499*, 419–425.
3. Wang, Q. H.; Kalantar-Zadeh, K.; Kis, A.; Coleman, J. N.; Strano, M. S. Electronics and Optoelectronics of Two-dimensional Transition Metal Dichalcogenides. *Nat. Nanotechnol.* **2012**, *7*, 699–712.
4. Chhowalla, M.; Shin, H. S.; Eda, G.; Li, L. J.; Loh, K. P.; Zhang, H. The Chemistry of Two-Dimensional Layered Transition Metal Dichalcogenide Nanosheets. *Nat. Chem.* **2013**, *5*, 263–275.
5. Mak, K. F.; Lee, C.; Hone, J.; Shan, J.; Heinz, T. F. Atomically Thin MoS_2: A New Direct-Gap Semiconductor. *Phys. Rev. Lett.* **2010**, *105*, 136805.
6. Zhao, W. J.; Ribeiro, R. M.; Toh, M. L.; Carvalho, A.; Kloc, C.; Neto, A. H. C.; Eda, G. Origin of Indirect Optical Transitions

in Few-Layer MoS_2, WS_2, and WSe_2. *Nano Lett.* **2013**, *13*, 5627–5634.
7. Radisavljevic, B.; Kis, A. Mobility Engineering and a Metal-Insulator Transition in Monolayer MoS_2. *Nat. Mater.* **2013**, *12*, 815–820.
8. Radisavljevic, B.; Radenovic, A.; Brivio, J.; Giacometti, V.; Kis, A. Single-Layer MoS_2 Transistors. *Nat. Nanotechnol.* **2011**, *6*, 147–150.
9. Radisavljevic, B.; Kis, A. Measurement of Mobility in Dual-Gated MoS_2 Transistors. *Nat. Nanotechnol.* **2013**, *8*, 147–148.
10. Bertolazzi, S.; Brivio, J.; Kis, A. Stretching and Breaking of Ultrathin MoS_2. *ACS Nano* **2011**, *5*, 9703–9709.
11. Peimyoo, N.; Shang, J. Z.; Cong, C. X.; Shen, X. N.; Wu, X. Y.; Yeow, E. K. L.; Yu, T. Nonblinking, Intense Two-Dimensional Light Emitter: Mono Layer WS_2 Triangles. *ACS Nano* **2013**, *7*, 10985–10994.
12. Georgiou, T.; Jalil, R.; Belle, B. D.; Britnell, L.; Gorbachev, R. V.; Morozov, S. V.; Kim, Y. J.; Gholinia, A.; Haigh, S. J.; Makarovsky, O.; et al. Vertical Field-Effect Transistor Based on Graphene-WS_2 Heterostructures for Flexible and Transparent Electronics. *Nat. Nanotechnol.* **2013**, *8*, 100–103.
13. Huo, N.; Kang, J.; Wei, Z.; Li, S.-S.; Li, J.; Wei, S.-H. Novel and Enhanced Optoelectronic Performances of Multilayer MoS_2–WS_2 Heterostructure Transistors. *Adv. Funct. Mater.* **2014**, *24*, 7025–7031.
14. Withers, F.; Bointon, T. H.; Hudson, D. C.; Craciun, M. F.; Russo, S. Electron Transport of WS_2 Transistors in a Hexagonal Boron Nitride Dielectric Environment. *Sci. Rep.* **2014**, *4*, 4967.
15. Liu, X.; Hu, J.; Yue, C.; Della Fera, N.; Ling, Y.; Mao, Z.; Wei, J. High Performance Field-Effect Transistor Based on Multilayer Tungsten Disulfide. *ACS Nano* **2014**, *8*, 10396–10402.
16. Ovchinnikov, D.; Allain, A.; Huang, Y. S.; Dumcenco, D.; Kis, A. Electrical Transport Properties of Single-Layer WS_2. *ACS Nano* **2014**, *8*, 8174–8181.
17. Braga, D.; Lezama, I. G.; Berger, H.; Morpurgo, A. F. Quantitative Determination of the Band Gap of WS_2 with Ambipolar Ionic Liquid-Gated Transistors. *Nano Lett.* **2012**, *12*, 5218–5223.
18. Yang, L.; Majumdar, K.; Liu, H.; Du, Y.; Wu, H.; Hatzistergos, M.; Hung, P. Y.; Tieckelmann, R.; Tsai, W.; Hobbs, C.; et al. Chloride Molecular Doping Technique on 2D Materials: WS_2 and MoS_2. *Nano Lett.* **2014**, *14*, 6275–6280.
19. Voiry, D.; Yamaguchi, H.; Li, J. W.; Silva, R.; Alves, D. C. B.; Fujita, T.; Chen, M. W.; Asefa, T.; Shenoy, V. B.; Eda, G.; et al. Enhanced Catalytic Activity in Strained Chemically Exfoliated WS_2 Nanosheets for Hydrogen Evolution. *Nat. Mater.* **2013**, *12*, 850–855.
20. Nicolosi, V.; Chhowalla, M.; Kanatzidis, M. G.; Strano, M. S.; Coleman, J. N. Liquid Exfoliation of Layered Materials. *Science* **2013**, *340*, 1226419.
21. Gutierrez, H. R.; Perea-Lopez, N.; Elias, A. L.; Berkdemir, A.; Wang, B.; Lv, R.; Lopez-Urias, F.; Crespi, V. H.; Terrones, H.; Terrones, M. Extraordinary Room-Temperature Photoluminescence in Triangular WS_2 Monolayers. *Nano Lett.* **2013**, *13*, 3447–3454.
22. Song, J. G.; Park, J.; Lee, W.; Choi, T.; Jung, H.; Lee, C. W.; Hwang, S. H.; Myoung, J. M.; Jung, J. H.; Kim, S. H.; et al. Layer-Controlled, Wafer-Scale, and Conformal Synthesis of Tungsten Disulfide Nanosheets Using Atomic Layer Deposition. *ACS Nano* **2013**, *7*, 11333–11340.
23. Orofeo, C. M.; Suzuki, S.; Sekine, Y.; Hibino, H. Scalable Synthesis of Layer-controlled WS_2 and MoS_2 Sheets by Sulfurization of Thin Metal Films. *Appl. Phys. Lett.* **2014**, *105*, 083112.
24. Elias, A. L.; Perea-Lopez, N.; Castro-Beltran, A.; Berkdemir, A.; Lv, R. T.; Feng, S. M.; Long, A. D.; Hayashi, T.; Kim, Y. A.; Endo, M.; et al. Controlled Synthesis and Transfer of Large-Area WS_2 Sheets: From Single Layer to Few Layers. *ACS Nano* **2013**, *7*, 5235–5242.
25. Jung, Y.; Shen, J.; Liu, Y.; Woods, J. M.; Sun, Y.; Cha, J. J. Metal Seed Layer Thickness-Induced Transition From Vertical to Horizontal Growth of MoS_2 and WS_2. *Nano Lett.* **2014**, *14*, 6842–6849.
26. Morrish, R.; Haak, T.; Wolden, C. A. Low-Temperature Synthesis of n-Type WS_2 Thin Films *via* H_2S Plasma Sulfurization of WO_3. *Chem. Mater.* **2014**, *26*, 3986–3992.
27. Rong, Y. M.; Fan, Y.; Koh, A. L.; Robertson, A. W.; He, K.; Wang, S. S.; Tan, H. J.; Sinclair, R.; Warner, J. H. Controlling Sulphur Precursor Addition for Large Single Crystal Domains of WS_2. *Nanoscale* **2014**, *6*, 12096–12103.
28. Fu, Q.; Wang, W.; Yang, L.; Huang, J.; Zhang, J.; Xiang, B. Controllable Synthesis of High Quality Monolayer WS_2 on a SiO_2/Si Substrate by Chemical Vapor Deposition. *RSC Adv.* **2015**, *5*, 15795–5799.
29. Zhang, Y.; Zhang, Y. F.; Ji, Q. Q.; Ju, J.; Yuan, H. T.; Shi, J. P.; Gao, T.; Ma, D. L.; Liu, M. X.; Chen, Y. B.; et al. Controlled Growth of High-Quality Monolayer WS_2 Layers on Sapphire and Imaging Its Grain Boundary. *ACS Nano* **2013**, *7*, 8963–8971.
30. Cong, C. X.; Shang, J. Z.; Wu, X.; Cao, B. C.; Peimyoo, N.; Qiu, C.; Sun, L. T.; Yu, T. Synthesis and Optical Properties of Large-Area Single-Crystalline 2D Semiconductor WS_2 Monolayer from Chemical Vapor Deposition. *Adv. Opt. Mater.* **2014**, *2*, 131–136.
31. Okada, M.; Sawazaki, T.; Watanabe, K.; Taniguch, T.; Hibino, H.; Shinohara, H.; Kitaura, R. Direct Chemical Vapor Deposition Growth of WS_2 Atomic Layers on Hexagonal Boron Nitride. *ACS Nano* **2014**, *8*, 8273–8277.
32. Lee, Y. H.; Zhang, X. Q.; Zhang, W. J.; Chang, M. T.; Lin, C. T.; Chang, K. D.; Yu, Y. C.; Wang, J. T. W.; Chang, C. S.; Li, L. J.; et al. Synthesis of Large-Area MoS_2 Atomic Layers with Chemical Vapor Deposition. *Adv. Mater.* **2012**, *24*, 2320–2325.
33. Ling, X.; Lee, Y. H.; Lin, Y. X.; Fang, W. J.; Yu, L. L.; Dresselhaus, M. S.; Kong, J. Role of the Seeding Promoter in MoS_2 Growth by Chemical Vapor Deposition. *Nano Lett.* **2014**, *14*, 464–472.
34. Lee, Y. H.; Yu, L. L.; Wang, H.; Fang, W. J.; Ling, X.; Shi, Y. M.; Lin, C. T.; Huang, J. K.; Chang, M. T.; Chang, C. S.; et al. Synthesis and Transfer of Single-Layer Transition Metal Disulfides on Diverse Surfaces. *Nano Lett.* **2013**, *13*, 1852–1857.
35. Li, X. S.; Cai, W. W.; An, J. H.; Kim, S.; Nah, J.; Yang, D. X.; Piner, R.; Velamakanni, A.; Jung, I.; Tutuc, E.; et al. Large-Area Synthesis of High-Quality and Uniform Graphene Films on Copper Foils. *Science* **2009**, *324*, 1312–1314.
36. Shi, J.; Ma, D.; Han, G.-F.; Zhang, Y.; Ji, Q.; Gao, T.; Sun, J.; Song, X.; Li, C.; Zhang, Y.; et al. Controllable Growth and Transfer of Monolayer MoS_2 on Au Foils and Its Potential Application in Hydrogen Evolution Reaction. *ACS Nano* **2014**, *8*, 10196–10204.
37. Shi, J.; Yang, Y.; Zhang, Y.; Ma, D.; Wei, W.; Ji, Q.; Zhang, Y.; Song, X.; Gao, T.; Li, C.; et al. Monolayer MoS_2 Growth on Au Foils and On-Site Domain Boundary Imaging. *Adv. Funct. Mater.* **2015**, *25*, 842–849.
38. Song, I.; Park, C.; Hong, M.; Baik, J.; Shin, H. J.; Choi, H. C. Patternable Large-Scale Molybdenium Disulfide Atomic Layers Grown by Gold-Assisted Chemical Vapor Deposition. *Angew. Chem., Int. Ed.* **2014**, *53*, 1266–1269.
39. Gao, L. B.; Ren, W. C.; Xu, H. L.; Jin, L.; Wang, Z. X.; Ma, T.; Ma, L. P.; Zhang, Z. Y.; Fu, Q.; Peng, L. M.; et al. Repeated Growth and Bubbling Transfer of Graphene with Millimetre-Size Single-Crystal Grains Using Platinum. *Nat. Commun.* **2012**, *3*, 699.
40. de la Rosa, C. J. L.; Sun, J.; Lindvall, N.; Cole, M. T.; Nam, Y.; Löffler, M.; Olsson, E.; Teo, K. B. K.; Yurgens, A. Frame Assisted H_2O Electrolysis Induced H_2 Bubbling Transfer of Large Area Graphene Grown by Chemical Vapor Deposition on Cu. *Appl. Phys. Lett.* **2013**, *102*, 022101.
41. Tian, J. F.; Cao, H. L.; Wu, W.; Yu, Q. K.; Guisinger, N. P.; Chen, Y. P. Graphene Induced Surface Reconstruction of Cu. *Nano Lett.* **2012**, *12*, 3893–3899.
42. Wang, Y. L.; Cong, C. X.; Qiu, C. Y.; Yu, T. Raman Spectroscopy Study of Lattice Vibration and Crystallographic Orientation of Monolayer MoS_2 under Uniaxial Strain. *Small* **2013**, *9*, 2857–2861.
43. Rice, C.; Young, R. J.; Zan, R.; Bangert, U.; Wolverson, D.; Georgiou, T.; Jalil, R.; Novoselov, K. S. Raman-scattering

Measurements and First-principles Calculations of Strain-induced Phonon Shifts in Monolayer MoS_2. *Phys. Rev. B* **2013**, *87*, 081307.
44. Castellanos-Gomez, A.; Roldan, R.; Cappelluti, E.; Buscema, M.; Guinea, F.; van der Zant, H. S. J.; Steele, G. A. Local Strain Engineering in Atomically Thin MoS_2. *Nano Lett.* **2013**, *13*, 5361–5366.
45. Peimyoo, N.; Yang, W.; Shang, J.; Shen, X.; Wang, Y.; Yu, T. Chemically Driven Tunable Light Emission of Charged and Neutral Excitons in Monolayer WS_2. *ACS Nano* **2014**, *8*, 11320–11329.
46. Dhakal, K. P.; Duong, D. L.; Lee, J.; Nam, H.; Kim, M.; Kan, M.; Lee, Y. H.; Kim, J. Confocal Absorption Spectral Imaging of MoS_2: Optical Transitions Depending on the Atomic Thickness of Intrinsic and Chemically Doped MoS_2. *Nanoscale* **2014**, *6*, 13028–13035.
47. Shi, Y. M.; Huang, J. K.; Jin, L. M.; Hsu, Y. T.; Yu, S. F.; Li, L. J.; Yang, H. Y. Selective Decoration of Au Nanoparticles on Monolayer MoS_2 Single Crystals. *Sci. Rep.* **2013**, *3*, 1839.
48. Park, H.-Y.; Lim, M.-H.; Jeon, J.; Yoo, G.; Kang, D.-H.; Jang, S. K.; Jeon, M. H.; Lee, Y.; Cho, J. H.; Yeom, G. Y. Wide-Range Controllable n-Doping of Molybdenum Disulfide (MoS_2) through Thermal and Optical Activation. *ACS Nano* **2015**, *9*, 2368–2376.
49. Zhao, W. J.; Ghorannevis, Z.; Amara, K. K.; Pang, J. R.; Toh, M.; Zhang, X.; Kloc, C.; Tan, P. H.; Eda, G. Lattice Dynamics in Mono- and Few-Layer Sheets of WS_2 and WSe_2. *Nanoscale* **2013**, *5*, 9677–9683.
50. Kuc, A.; Zibouche, N.; Heine, T. Influence of Quantum Confinement on the Electronic Structure of the Transition Metal Sulfide TS_2. *Phys. Rev. B* **2011**, *83*, 245213.
51. Zhao, W. J.; Ghorannevis, Z.; Chu, L. Q.; Toh, M. L.; Kloc, C.; Tan, P. H.; Eda, G. Evolution of Electronic Structure in Atomically Thin Sheets of WS_2 and WSe_2. *ACS Nano* **2013**, *7*, 791–797.
52. Tongay, S.; Zhou, J.; Ataca, C.; Liu, J.; Kang, J. S.; Matthews, T. S.; You, L.; Li, J. B.; Grossman, J. C.; Wu, J. Q. Broad-Range Modulation of Light Emission in Two-Dimensional Semiconductors by Molecular Physisorption Gating. *Nano Lett.* **2013**, *13*, 2831–2836.
53. Mouri, S.; Miyauchi, Y.; Matsuda, K. Tunable Photoluminescence of Monolayer MoS_2 *via* Chemical Doping. *Nano Lett.* **2013**, *13*, 5944–5948.
54. Mak, K. F.; He, K. L.; Lee, C.; Lee, G. H.; Hone, J.; Heinz, T. F.; Shan, J. Tightly Bound Trions in Monolayer MoS_2. *Nat. Mater.* **2013**, *12*, 207–211.
55. Yang, L. M.; Majumdar, K.; Liu, H.; Du, Y. C.; Wu, H.; Hatzistergos, M.; Hung, P. Y.; Tieckelmann, R.; Tsai, W.; Hobbs, C.; et al. Chloride Molecular Doping Technique on 2D Materials: WS_2 and MoS_2. *Nano Lett.* **2014**, *14*, 6275–6280.
56. Chae, S. H.; Yu, W. J.; Bae, J. J.; Duong, D. L.; Perello, D.; Jeong, H. Y.; Ta, Q. H.; Ly, T. H.; Vu, Q. A.; Yun, M.; et al. Transferred Wrinkled Al_2O_3 for Highly Stretchable and Transparent Graphene-Carbon Nanotube Transistors. *Nat. Mater.* **2013**, *12*, 403–409.
57. Zhang, H. W.; Duan, G. T.; Liu, G. Q.; Li, Y.; Xu, X. X.; Dai, Z. F.; Wang, J. J.; Cai, W. P. Layer-Controlled Synthesis of WO_3 Ordered Nanoporous Films for Optimum Electrochromic Application. *Nanoscale* **2013**, *5*, 2460–2468.